PAPER

Check for updates

Dual-stimuli-responsive nanoparticles for the co-delivery of small molecules to promote neural differentiation of human iPSCs†

Jeong Hyun You,‡[a] Na Yeon Kim,‡[a] Yoon Young Choi,[b] Hyung Woo Choi[c] and Bong Geun Chung ●[ID] *[a,b,c,d]

The differentiation of human induced pluripotent stem cells (hiPSCs) into neural progenitor cells (NPCs) is a promising approach for the treatment of neurodegenerative diseases and regenerative medicine. Dual-SMAD inhibition using small molecules has been identified as a key strategy for directing the differentiation of hiPSCs into NPCs by regulating specific cell signaling pathways. However, conventional culture methods are time-consuming and exhibit low differentiation efficiency in neural differentiation. Nanocarriers can address these obstacles as an efficient platform for the controlled release and accurate delivery of small molecules. In this paper, we developed calcium phosphate-coated mesoporous silica nanoparticles capable of delivering multiple small molecules, including LDN193189 as a bone morphogenetic protein (BMP) inhibitor and SB431542 as a transforming growth factor (TGF)-beta inhibitor, for direct differentiation of hiPSC-mediated NPCs. Our results demonstrated that this nanocarrier-mediated small molecule release system not only enhanced the *in vitro* formation of neural rosettes but also modulated the expression levels of key markers. In particular, it downregulated OCT4, a marker of pluripotency, while upregulating PAX6, a critical marker for the neuroectoderm. These findings suggest that this controlled small molecule release system holds significant potential for therapeutic applications in neural development and neurodegenerative diseases.

1. Introduction

Efficient conversion of human induced pluripotent stem cells (hiPSCs) into neural progenitor cells (NPCs) holds significant importance in neurodegenerative therapy and neurological disease research.[1,2] Patient-derived iPSCs offer a number of advantages, such as immunological compatibility and ethical considerations. NPCs, possessing the ability to differentiate into various neural cell types (*e.g.*, neurons,[3] astrocytes,[4] and oligodendrocytes[5]), are promising tools for cell-based therapies. In the past, neural induction protocols have involved intricate steps, such as embryoid body formation or stromal feeder co-culture.[6] These methods are still time-consuming, labor-intensive, and costly.[7] Despite recent advancements in neural differentiation protocols, the challenges persist in achieving high efficiency and precision in generating specific neural lineages. A number of new approaches, such as chemically defined media or substrate-based induction, have reduced variability but still suffer from limited scalability and consistency in generating mature neural subtypes.[8–10] Thus, there remains a pressing need for more robust methods capable of directing stem cell differentiation with minimal off-target effects.

Stem cells are highly responsive to chemical signals in their microenvironments, such as growth factors, cytokines, and small molecules, which influence their differentiation fate.[11,12] Signaling molecules, such as BMP and Wnt, activate key pathways, including SMAD, Notch, and Wnt/β-catenin, which are essential for promoting neural differentiation.[13–16] Among the BMP and TGF-β signaling inhibitors, LDN193189 and SB431542 were chosen for their well-established roles in enhancing neural differentiation. LDN193189 selectively inhibits BMP-type I receptors to suppress SMAD1/5/9 activation, while SB431542 targets TGF-β type I receptors to reduce SMAD2/3 activity. These combined effects promote neuroectodermal differentiation while minimizing mesoderm and glial lineage induction. During embryonic development, neural ectoderm differentiation is driven by the suppression of mesoderm and endoderm formation[17] and a process can be regu-

[a]Department of Biomedical Engineering, Sogang University, Seoul 04107, Korea. E-mail: bchung@sogang.ac.kr
[b]Institute of Integrated Biotechnology, Sogang University, Seoul 04107, Korea
[c]Department of Mechanical Engineering, Sogang University, Seoul 04107, Korea
[d]Institute of Smart Biosensor, Sogang University, Seoul 04107, Korea
†Electronic supplementary information (ESI) available. See DOI: https://doi.org/10.1039/d4nr04413d
‡These authors contributed equally to this work.

lated by BMP and TGF-β signaling. These pathways initiate signal transduction by binding to cell surface receptors, leading to the phosphorylation of intracellular SMAD proteins, which translocate to the nucleus to regulate target gene expression.[18,19] The inhibition of specific signaling pathways has proved to be a powerful strategy for enhancing differentiation efficiency and selectively directing cell fate, with broad applications in cell therapy and tissue engineering.[20] However, the traditional methods of adding signaling inhibitors directly to culture media are often inefficient and can lead to cytotoxicity or immune responses at higher concentrations. To address these challenges, nanoparticle-based delivery systems offer a more targeted approach, enabling precise and controlled release of differentiation factors, thereby improving efficiency and reducing adverse effects.[21,22] Nanoparticle-based delivery systems have gained significant attention in stem cell research for their ability to not only enhance differentiation but also improve stem cell survival, integration, and functional maturation following transplantation.[23] Recent advancements in nanoparticle-mediated gene and protein delivery have enabled precise control over stem cell fate and function in both *in vitro* and *in vivo* models. Among these, mesoporous silica nanoparticles (MSNs) stand out due to their high surface area, biocompatibility, and versatility in surface functionalization, making them ideal candidates for drug delivery systems (DDSs).[24] A key advantage of MSNs lies in their ability to release encapsulated cargo in a controlled manner, responding to specific cellular cues, such as pH, redox conditions, or enzymatic activity. This controlled release can be tailored by adjusting the properties of MSNs or incorporating stimuli-responsive elements.[25] For instance, simultaneous condensation of multiple silica precursors allows for precise control over pore size and structure, enabling the introduction of functional groups on the MSN surface.[26] pH-responsive MSNs are particularly effective in acidic environments, such as tumor tissues or intracellular lysosomes, where they can release their contents efficiently. Additionally, calcium phosphate (CaP), a biodegradable and biocompatible compound, is often integrated with MSNs for its pH sensitivity, dissolving more readily under acidic conditions.[27,28] Disulfide bonds, cleavable in the presence of glutathione (GSH), a tripeptide found in intracellular environments, can also be incorporated into MSN structures, allowing for cargo release under reductive cellular conditions.[29,30] Dual-stimuli-responsive delivery systems, which respond to multiple triggers, such as pH and redox changes, offer enhanced precision by allowing more accurate and efficient drug release compared to conventional systems.[31] These systems hold great potential for advancing targeted drug delivery and improving therapeutic outcomes.[32]

Our study investigates the effect of nanoparticle-mediated dual-small molecule delivery on neural differentiation in stem cells. Specifically, we introduce a dual-SMAD inhibition strategy using two small molecules that selectively inhibit the transforming growth factor (TGF)-β and bone morphogenetic protein (BMP) signaling pathways. MSNs are employed as carriers to deliver these molecules with CaP acting as gatekeepers and GSH-sensitive disulfide bonds within the MSN structure controlling the release of the encapsulated agents. While SMAD inhibition has widely been used to induce neural differentiation, the novelty of our approach lies in the dual-stimuli-responsive MSN-CaP system. This system allows for the spatiotemporal control of small molecule release in response to both pH and GSH levels, providing enhanced precision compared to conventional methods that rely on continuous exposure to inhibitors. These traditional methods can lead to off-target effects and potential toxicity. Our system ensures that differentiation signals are specifically released in cellular environments favorable for neural differentiation. We expect that the controlled release of LDN193189 and SB431542 from the MSN-CaP system in response to these dual stimuli can lead to faster and more accurate generation of specific neural precursor cell types compared to conventional methods. Moreover, precise control over differentiation provided by the MSN-CaP system could reduce risks associated with current stem cell therapies, such as incomplete differentiation, tumorigenicity, and immune rejection. By enabling more targeted and efficient neural differentiation, this method holds significant promise for safer and more effective treatments of neurological disorders including neurodegenerative diseases, spinal cord injuries, and ischemic strokes.

2. Results and discussion

2.1. Physicochemical characterization of MSN-CaP

We designed dual-stimuli-responsive MSN-CaP nanoparticles for the co-delivery of small molecules (Scheme 1).

Transmission electron microscopy (TEM) analysis confirmed that MSNs showed a uniform spherical morphology with an average size of about 100 nm (Fig. 1A). BTES addition contributed to the pore expansion of the porous nanoparticles,[30] resulting in a rough surface morphology. After CaP coating, the spherical morphology of the nanoparticles was maintained, but the surface became smoother and more uniform. Additionally, the average size of the nanoparticles increased to about 110 nm, which was attributed to the formation of a CaP coating layer. Energy dispersive X-ray spectroscopy (EDS) showed that the nanoparticles were composed of Si, O, Ca, S, and P elements with the respective contents of 50.37% Si, 41.15% O, 6.63% Ca, 1.67% S, and 0.18% P (Fig. 1B). This confirmed that Si and O were uniformly distributed throughout the nanoparticles, while the S element was present in a relatively small amount, which was attributed to the tetrasulfide structure of BTES. The presence of Ca and P elements revealed that CaP was coated on the MSN surface.

DLS analysis showed that the average size of MSNs was 102 nm, while the average size of MSN-CaP was 166 nm (Fig. 2A). The distribution of particle sizes was found to be uniform with differential numbers at peaks of 15–20%. DLS was used to measure the hydrodynamic diameter of the nano-
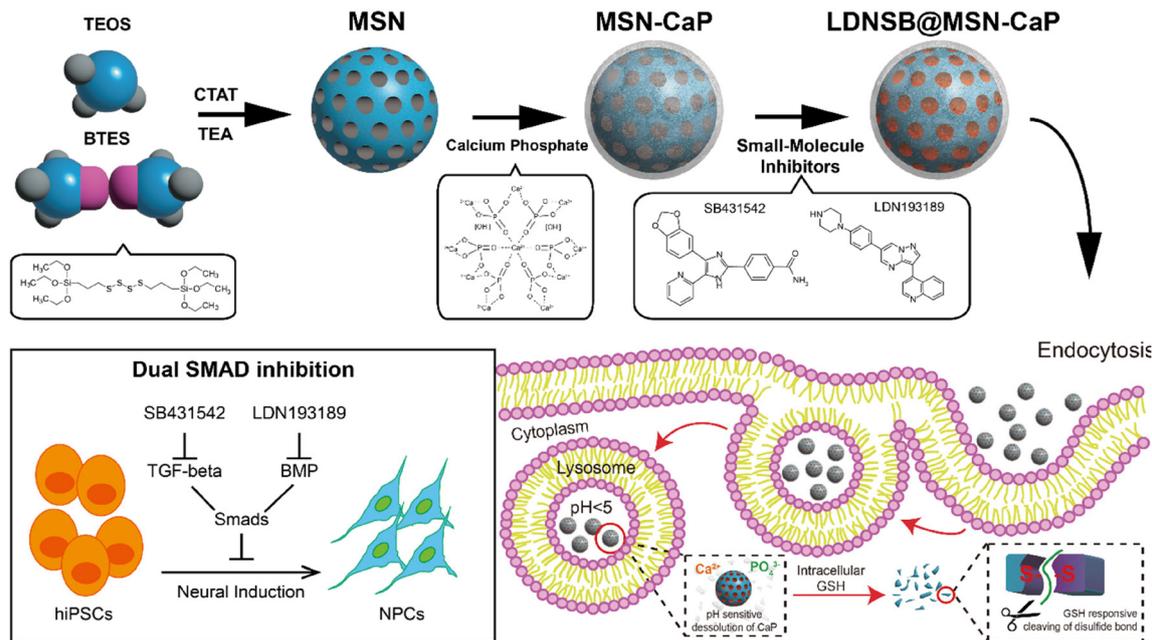
Scheme 1 Schematic drawing of the dual-stimuli-responsive MSN-CaP nanoparticles for the co-delivery of small molecules for hiPSC-mediated neural differentiation.
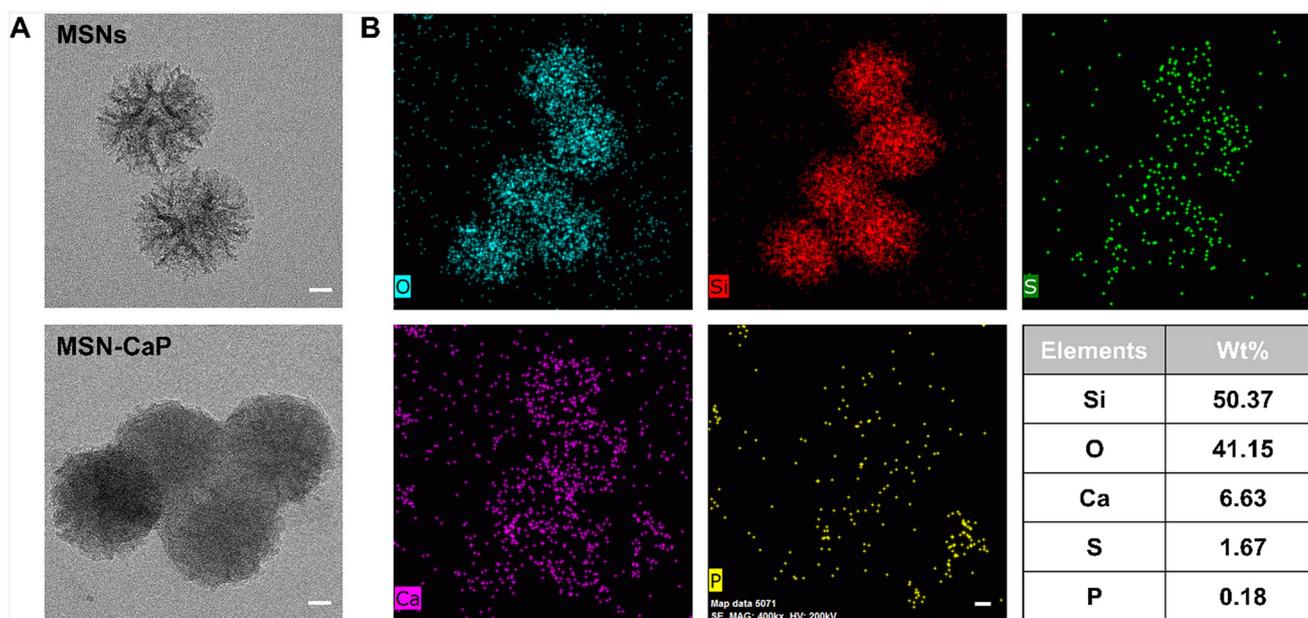

Fig. 1 (A) Transmission electron microscopy (TEM) images and (B) energy dispersive X-ray spectroscopy (EDS) maps of MSN-CaP nanoparticles. The scale bars are 20 nm.

particles in solution, which often appears larger than the core diameter measured using TEM analysis in a dry state. The analysis confirmed that the average particle size increased after the formation of a CaP coating layer on the MSN surface. N_2 adsorption–desorption analysis was performed to investigate the specific surface area, pore volume, and pore size distribution of MSNs and MSN-CaP (Fig. 2B). The adsorption–de-

sorption curve exhibited the characteristic type IV isotherm shape typical of mesoporous materials. Additionally, the steep and narrow H1 hysteresis loop shape indicated the formation of a narrow range of homogeneous mesopores.[33] Comparing the adsorption amounts across all relative pressure regions, we observed that the adsorption amount of MSN-CaP was lower than that of MSNs. This reduction is attributed to the decrease
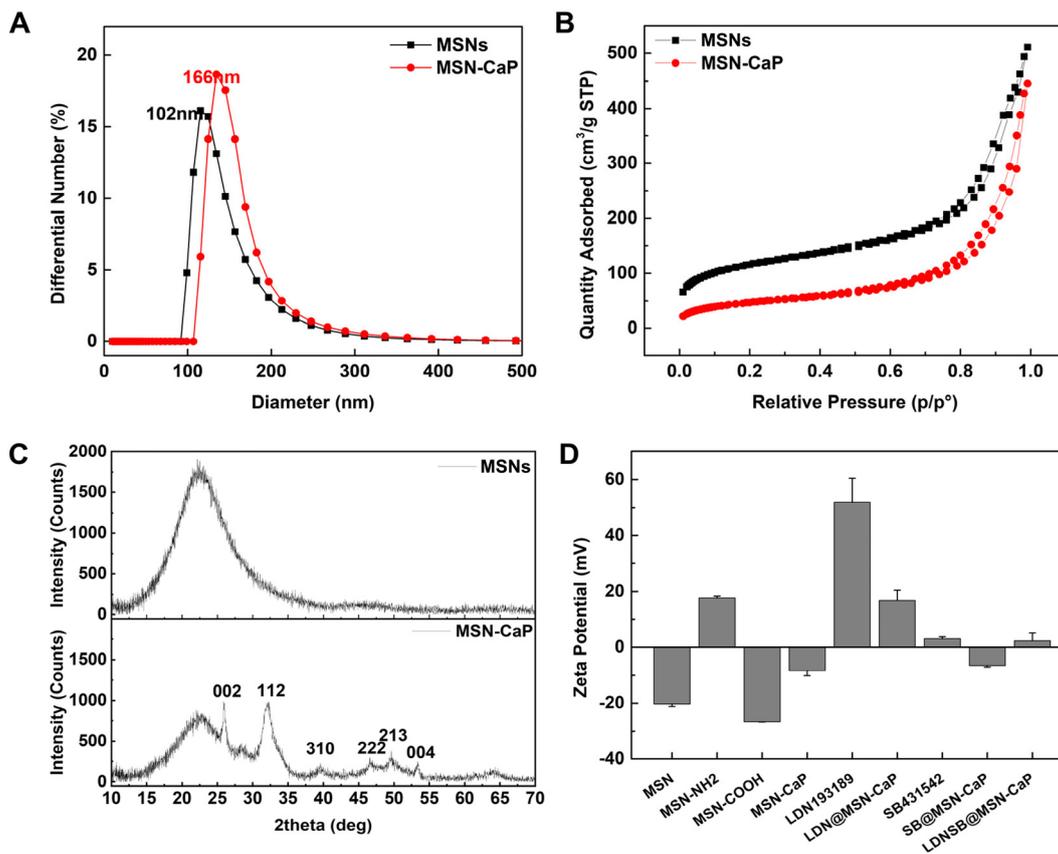
Fig. 2 Physiochemical analysis of MSN–CaP nanoparticles. (A) Average hydrodynamic diameters of MSNs and MSN–CaP nanoparticles analyzed using DLS. (B) N_2 adsorption/desorption isotherms of the MSNs and MSN–CaP nanoparticles. (C) XRD patterns of MSNs and MSN–CaP nanoparticles. (D) Zeta potential value of MSNs, MSN-NH$_2$, MSN-COOH, MSN–CaP, LDN193189, LDN@MSN–CaP, SB431542, SB@MSN–CaP and LDNSB@MSN–CaP nanoparticles.

in the specific surface area and pore volume of MSNs caused by CaP coating. According to the BET analysis, the specific surface area of MSNs was found to be 419.0939 m^2 g^{-1}, whereas MSN–CaP exhibited a reduced specific surface area of 170.6921 m^2 g^{-1}. The total pore volume was determined to be 0.7907 cm^3 g^{-1} for MSNs and 0.6888 cm^3 g^{-1} for MSN–CaP. N$_2$ adsorption–desorption analysis confirmed that CaP coating reduced the surface area of MSNs, thereby contributing to the decrease in pore volume. XRD results demonstrated successful coating of CaP on the MSN surface (Fig. 2C). The broad peak near 22° in the X-ray diffraction pattern of the MSNs indicates a characteristic scattering pattern of an amorphous structure, lacking a specific crystalline arrangement. This pattern persisted even after the CaP coating, confirming the retention of the amorphous structure. The XRD analysis of MSN–CaP reveals characteristic peaks corresponding to hydroxyapatite ($Ca_{10}(PO_4)_6(OH)_2$), a type of calcium phosphate, based on JCPDS card number 09-0432. The peaks at 25.9°, 32°, 39.6°, 47°, 49.6°, and 53.3° correspond to the (002), (211), (130), (222), (213), and (004) planes, the main crystal facets of hydroxyapatite, respectively. From the intensity and sharpness of the peaks, the high crystallinity of the formed CaP can be inferred.[34,35] The zeta potential measurements indicate the

change in surface properties, confirming the successful surface modification and entrapment of small molecules (Fig. 2D). MSNs dispersed in water exhibited negative charge with a zeta potential of −20.22 mV. Introducing an amine group significantly increased the surface charge of MSN-NH$_2$ to a positive value of 17.53 mV, whereas introducing a carboxyl group resulted in a strong negative charge of −26.73 mV for MSN-COOH. The surface charge of MSN–CaP increased to −8.35 mV, indicating the successful coating of CaP. MSN–CaP is a negatively charged nanocarrier, whereas LDN193189 is a positively charged small molecule with a high surface charge of 51.72 mV. We observed a significant increase in the surface charge of LDN@MSN–CaP to 16.64 mV, indicating the successful encapsulation of LDN193189 within MSN–CaP *via* electrostatic interactions. SB431542 is a small molecule with a weak positive charge of 2.95 mV, and the surface charge of SB@MSN–CaP changed slightly to −6.48 mV, indicating that it was enclosed by attraction with MSN–CaP. The zeta potential of MSN–CaP nanoparticles encapsulating both LDNs and SBs simultaneously changed to 2.47 mV. The surface charges of LDN and SB offset the negative charge of MSN–CaP, resulting in a weak positive charge, indicating that LDN and SB were successfully co-encapsulated.

2.2. Analysis of small molecule content and pH/GSH dual-stimuli-responsive release behavior

Standard curves were constructed to determine the relationship between the concentration and absorbance values of each small molecule. For LDN, a linear relationship (R^2 = 0.9983) was observed between the absorbance (λ = 230 nm) and concentration (Fig. S1A†). For SB too, a linear relationship was observed (R^2 = 0.998) between the absorbance (λ = 323 nm) and concentration (Fig. S1B†). Standard curves were used to quantitatively analyze the content of loaded small molecules in MSN-CaP. The encapsulation efficiency of LDN@MSN-CaP was 96.62% with a loading capacity of 5.28%, while SB@MSN-CaP showed an encapsulation efficiency of 99.28% with a loading capacity of 4.55%. In LDNSB@MSN-CaP, where both small molecules were co-encapsulated, the loading capacities were calculated to be 5.22% for LDN and 4.30% for SB.

$$\text{Encapsulation efficiency (EE\%)}$$
$$= \frac{\text{Total small molecule added} - \text{Free small molecule}}{\text{Total small molecule added}} \times 100(\%)$$

$$\text{Loading capacity (LC\%)}$$
$$= \frac{\text{Total encapsulated small molecule}}{\text{Total nanoparticle weight}} \times 100(\%)$$

To evaluate the release of small molecules under conditions simulating extracellular (pH 7.4) and intracellular endosomes and lysosomes (pH 5), LDN@MSN-CaP, SB@MSN-CaP, and LDNSB@MSN-CaP were incubated at pH 5 and 7.4. The amount of LDN released from LDN@MSN-CaP over 24 hours at pH 5 was 79.3%, which was approximately 2.93 times more than at pH 7.4, where 27.1% was released (Fig. 3A). The amount of SB released from SB@MSN-CaP was 76.4% in the acidic environment, which was about 2.97 times more than in the neutral environment, where 25.7% was released (Fig. 3B). For LDNSB@MSN-CaP, approximately 1.90-fold (64.9% vs. 34.2%) more LDN was released and approximately 1.75-fold (56.2% vs. 32.2%) more SB was released at pH 5 compared to pH 7.4 conditions (Fig. 3C). The discrepancy in release rates between LDNSB@MSN-CaP and single drug-loaded nanoparticles (LDN@MSN-CaP and SB@MSN-CaP) is probably due to subtle interactions between LDN and SB within the dual-loading system and the differences in their loading environments. Despite these minor variations, LDNSB@MSN-CaP exhibited comparable loading efficiencies for both LDN and SB, confirming that the dual-loading system could stably encapsulate both compounds. Importantly, the cumulative release of LDN was consistently higher than that of SB under all pH conditions, mirroring the trends observed in single-drug systems, indicating that the intrinsic properties of each compound are preserved in the dual-loading system. These results validate the functionality of MSN-CaP nanoparticles as a robust pH-responsive delivery platform. This suggests that CaP-coated MSNs could serve as pH-sensitive delivery vehicles for the controlled release of small molecules. Previous studies have reported similar findings, demonstrating that CaP coatings degrade under acidic conditions, enabling the controlled release of encapsulated cargo, such as therapeutic drugs or sig-
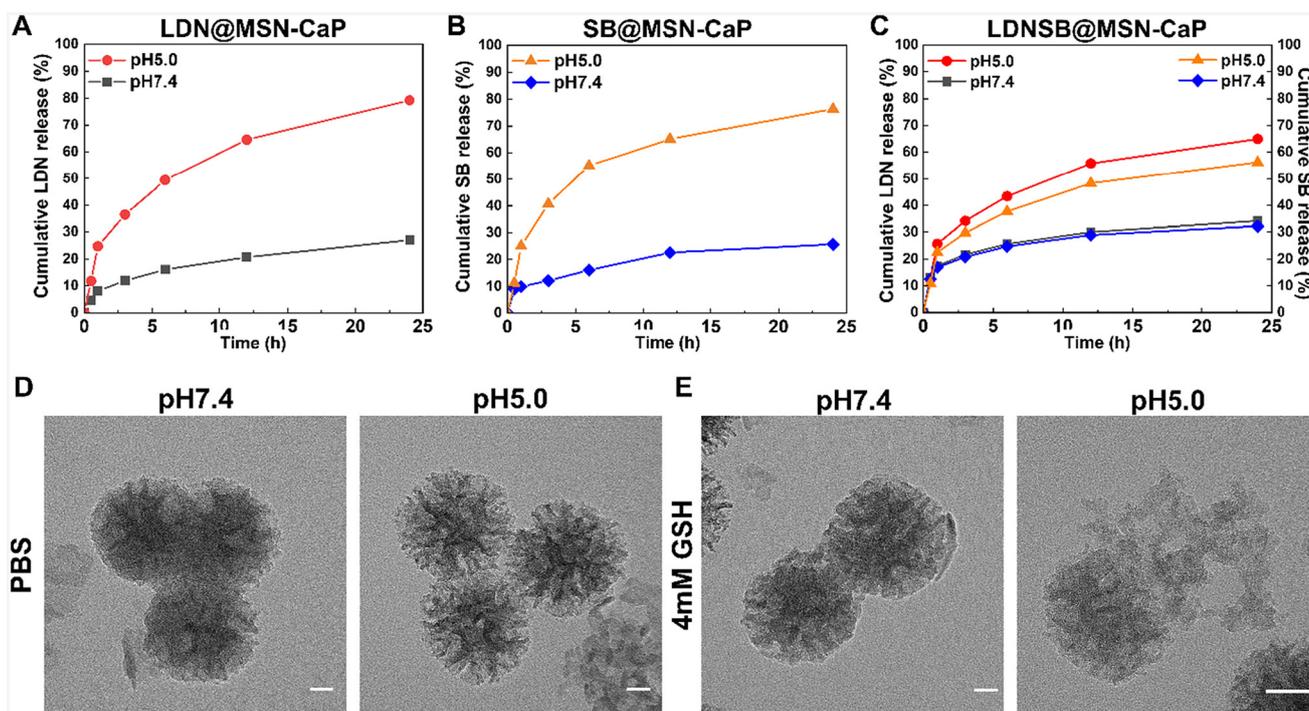

Fig. 3 Dual-stimuli-responsive analysis of MSN-CaP nanoparticles. (A–C) Release profiles of LDN@MSN-CaP, SB@MSN-CaP, and LDNSB@MSN-CaP nanoparticles. (D and E) TEM images of MSN-CaP morphology under various acidity and GSH treatment conditions. The scale bars are 20 nm.

naling molecules within intracellular environments.[27,28] These results align with our observations and further validate the potential of CaP-coated MSNs as efficient pH-sensitive delivery systems, particularly for applications in neural differentiation. Furthermore, the accelerated release of LDN and SB in acidic environments aligns with the typical pH conditions of intracellular lysosomes (~pH 5.0). This ensures targeted release within stem cells after nanoparticle internalization, as confirmed by the colocalization of MSN-CaP nanoparticles with lysosomes in confocal imaging (Fig. 5). Such pH-triggered degradation minimizes premature release under neutral extracellular conditions while enhancing intracellular delivery efficiency. TEM analysis was employed to visualize the pH- and GSH-induced morphological changes of MSN-CaP nanoparticles (Fig. 3D). Under pH 7.4 conditions, the CaP coating layer remained stable and the pores on the nanoparticle surface were closed. However, under pH 5 conditions, the CaP coating layer was collapsed to show large pores on the nanoparticle surface. These results indicate that the solubility of the CaP coating layer increases in the acidic environment. Furthermore, the changes in the nanoparticle morphology were also observed with GSH treatment. Under pH 7.4 conditions, the morphology of the nanoparticles in response to GSH treatment did not show any significant changes. This stability is attributed to the CaP coating layer remaining unchanged and structurally stable at pH 7.4. On the other hand, the morphology of the nanoparticles was completely collapsed after GSH treatment at pH 5, revealing their internal structure. It is probably due to GSH cleaving the tetrasulfide bonds inside the MSNs, leading to the collapse of the structural stability.[36] These results demonstrate the potential of MSN-CaP nanoparticles as a pH/GSH dual-stimuli-responsive drug delivery system: under pH 7.4 conditions, the stable CaP coating layer prevents small molecule leakage, whereas under pH 5 conditions, GSH treatment induces nanoparticle morphology collapse, facilitating small molecule release.

2.3. Biocompatibility analysis of the nanoparticles

To investigate the optimal concentration for safe and effective small molecule delivery, we assessed the biocompatibility of LDN@MSN-CaP, SB@MSN-CaP, and LDNSB@MSN-CaP at hiPSC concentrations ranging from 2 to 50 μg mL^{-1} using the MTT assay. LDN@MSN-CaP maintained more than 85% cell viability only at concentrations below 10 μg mL^{-1}, with lower cell viabilities of 52.3% at 25 μg mL^{-1} and 7.55% at 50 μg mL^{-1} (Fig. 4A). This could be attributed to the toxicity of LDN itself or potential cell damage caused by the increased intracellular penetration of LDN@MSN-CaP. However, at concentrations below 10 μg mL^{-1}, we anticipate low cytotoxicity and efficient small molecule delivery. SB@MSN-CaP was found to be highly safe, maintaining a cell viability of >80% across all concentrations (Fig. 4B). LDNSB@MSN-CaP showed more than 80% cell viability in the concentration range of 2–25 μg mL^{-1}, but showed a lower cell viability of 8.4% at 50 μg mL^{-1} (Fig. 4C). Based on these cell viability results, a concentration of 10 μg mL^{-1} was chosen for further study, as it exhibited no apparent toxicity to hiPSCs.

Next, we evaluated the intracellular uptake and distribution of pH-sensitive MSN-CaP nanoparticles, which were designed to release their loaded small molecules in an acidic environment similar to intracellular endosomes and lysosomes. To achieve this, we labelled the MSN-CaP nanoparticles without loaded small molecules with the FITC fluorescent dye, stained them with LysoTracker®, which specifically stains the lysosomes (the acidic compartments) of hiPSCs, and observed them under a confocal microscope (Fig. 5). As a result, the FITC-labeled MSN-CaP nanoparticles were clearly observed after treatment with hiPSCs, indicating that the nanoparticles could effectively penetrate the cell membrane. Notably, the FITC-labeled MSN-CaP nanoparticles were observed not only in the cytoplasm and cell nucleus but also in the lysosome compartments stained with LysoTracker®, as confirmed by the overlapping and spatial coincidence of the two fluorescence signals (white arrow). These results demonstrated that MSN-CaP nanoparticles were successfully delivered and accumulated in the targeted location, specifically within lysosomes, which were characterized by an acidic intracellular environment.

2.4. Effect of small molecule-encapsulated nanoparticles on neural induction

To investigate the effect of small molecule-loaded nanoparticles on neural differentiation, we treated undifferentiated
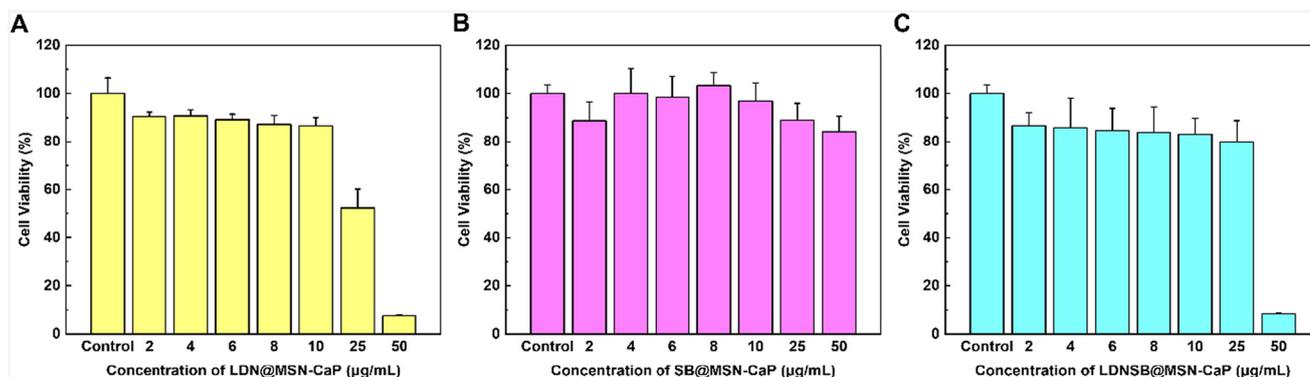

Fig. 4 Cytotoxicity evaluation of LDN@MSN-CaP, SB@MSN-CaP, and LDNSB@MSN-CaP nanoparticles in hiPSCs. (A–C) Quantitative analysis of the viability of LDN@MSN-CaP, SB@MSN-CaP, and LDNSB@MSN-CaP nanoparticles in hiPSCs.
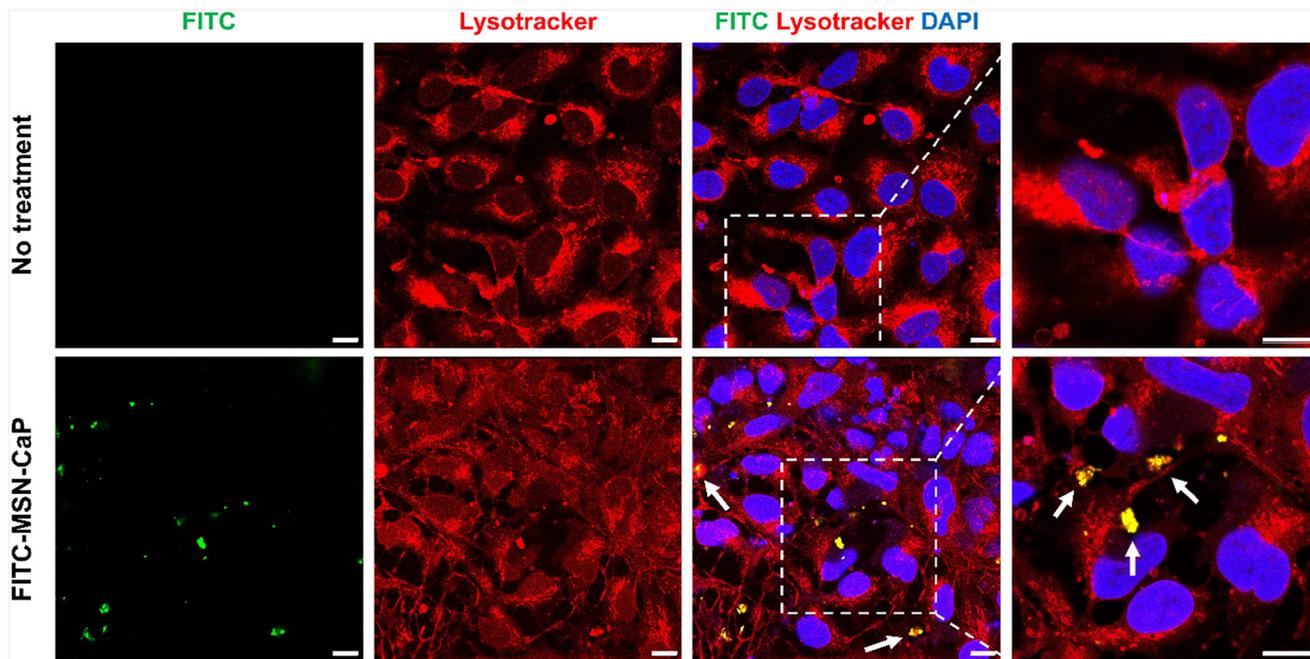
Fig. 5 Evaluation of the intracellular lysosome uptake of FITC-labeled MSN-CaP nanoparticles. Confocal imaging of FITC (green) and LysoTracker® (red) in hiPSCs treated with 20 μg mL^{-1} of MSN-CaP for 24 hours. The images show the subcellular localization of FITC in lysosomes (white arrow). LysoTracker® Red stains the lysosomes. The scale bars are 50 μm.

hiPSCs with various combinations of nanoparticles and evaluated their potential to induce neural differentiation and rosette structure formation. hiPSCs were treated with LDN@MSN-CaP, SB@MSN-CaP, and LDNSB@MSN-CaP nanoparticles for 1 day or 5 days (Fig. 6A). Immunofluorescence analysis was performed to evaluate the expression of OCT4, a pluripotency marker, and PAX6, a neural progenitor marker, in response to different nanoparticle formulations. As shown in Fig. 6B, on day 1, the control cells maintained high OCT4 expression with minimal PAX6 expression, indicating preserved pluripotency. In contrast, the cells treated with LDN@MSN-CaP, SB@MSN-CaP, and LDNSB@MSN-CaP exhibited a notable decrease in OCT4 expression and a corresponding increase in PAX6 expression, with the LDNSB@MSN-CaP group showing the most significant changes.

On day 5, the cells treated with LDNSB@MSN-CaP began to form rosette structures, characteristic of neural progenitor differentiation, accompanied by a substantial increase in PAX6 expression localized within the rosette regions. The formation of these rosettes was most pronounced in the LDNSB@MSN-CaP group, where PAX6-positive cells were highly organized into distinct circular patterns. Quantitative analysis (Fig. 6C) demonstrated that on day 1, PAX6 expression increased approximately 3.2-fold ($p < 0.001$) in the LDNSB@MSN-CaP group compared to controls, while OCT4 expression decreased by 1.5-fold ($p < 0.001$). On day 5, PAX6 expression showed a near 15-fold increase ($p < 0.001$) and OCT4 expression showed a 4.8-fold decrease ($p < 0.001$) in the LDNSB@MSN-CaP group relative to the controls. The emer-

gence of the rosette structures, particularly in the LDNSB@MSN-CaP group, correlates with elevated PAX6 expression, suggesting that these nanoparticle formulations, especially LDNSB@MSN-CaP, not only promote neural differentiation but also facilitate the organization of cells into rosette structures, indicative of advanced neural progenitor differentiation. These results highlight the differential effects of the nanoparticle formulations on stem cell-mediated neural differentiation, with a particular emphasis on neural rosette formation, an essential marker of early neural differentiation. The substantial reduction in OCT4 expression and the marked increase in PAX6 expression in the LDNSB@MSN-CaP-treated group indicate that dual-inhibition nanoparticles are more effective in driving pluripotent stem cells towards a neural progenitor fate than mono-inhibition formulations. The prominent rosette formation in this group further underscores the potential of LDNSB@MSN-CaP to promote neural lineage commitment. Neural rosettes are radial arrangements of NPCs that resemble the neural tube, a critical structure in central nervous system development.[37] In this study, the LDNSB@MSN-CaP group demonstrated the most robust rosette formation, suggesting a more efficient activation of neural differentiation pathways. This enhanced effect is probably attributable to the synergistic action of LDN193189, a BMP inhibitor, and SB431542, a TGF-β receptor inhibitor, encapsulated within MSN-CaP nanoparticles. By simultaneously inhibiting both BMP and TGF-β signaling pathways, LDNSB@MSN-CaP creates a microenvironment conducive to neural lineage commitment and neural tube-like structure formation, as evidenced by the enhanced rosette formation. On
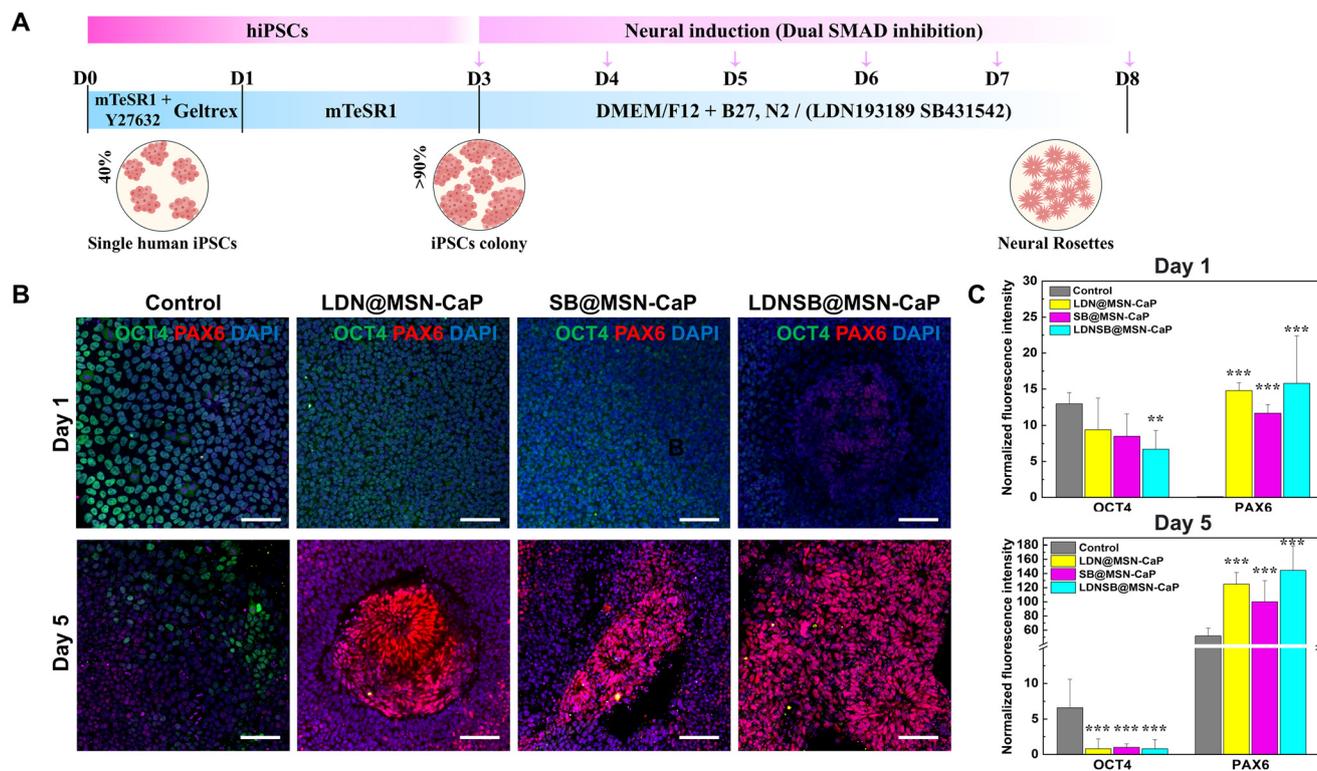
Fig. 6 Effect of the small molecule-encapsulated MSN-CaP nanoparticles on the neural induction of hiPSCs. (A) Protocol for inducing neural differentiation in hiPSCs with nanoparticle treatment. It shows the neural differentiation procedure for nanoparticle treatment for 1 day and 5 days. (B and C) Analysis of OCT4- and PAX6-positive cell intensities after treating with LDN@MSN-CaP, SB@MSN-CaP and LDNSB@MSN-CaP nanoparticles for 1 day and 5 days. Values are presented as mean ± SEM. Statistical significance is indicated as *$p < 0.05$, **$p < 0.01$, and ***$p < 0.001$ as determined by one-way ANOVA with Bonferroni's multiple comparison test. Scale bars are 50 μm.

day 5, the sustained and elevated PAX6 expression in the LDNSB@MSN-CaP group, along with pronounced rosette structures, contrasts with the less prominent effects observed in the LDN@MSN-CaP and SB@MSN-CaP groups. This synergistic effect stems from the ability of LDN193189 and SB431542 to precisely modulate SMAD1/5/9 and SMAD2/3 signaling pathways, respectively, thereby directing neural differentiation. The selection of these molecules was based on their robust performance in neural induction protocols and their ability to reduce off-target effects when delivered in a controlled manner using MSN-CaP nanoparticles. These findings underscore the critical role of simultaneous inhibition of multiple signaling pathways in driving efficient neural differentiation and fostering the structural organization of rosettes. The pH-responsive release mechanism of MSN-CaP nanoparticles ensures that LDN and SB are released predominantly within acidic intracellular compartments, facilitating the effective modulation of SMAD signaling pathways critical for neural differentiation. This targeted delivery mechanism reduces the risk of off-target effects and ensures a consistent and controlled differentiation process. From a clinical perspective, the enhanced efficiency and precision of neural differentiation observed in this study suggest promising applications in regenerative medicine. These include potential therapies for neurodegenerative diseases, such as Parkinson's or

Alzheimer's disease, where targeted neural induction is critical. The controlled release mechanism of the proposed system could also reduce the risks associated with off-target effects, a significant challenge in current stem cell therapies. The statistical significance ($p < 0.001$) of these observations further supports the robustness of the findings. From a biological perspective, the enhanced neuronal differentiation and rosette formation observed with LDNSB@MSN-CaP treatment is probably due to the precise regulation of the extracellular environment and intracellular signaling pathways.[38,39] These findings suggest that MSN-CaP nanoparticles co-loaded with LDN193189 and SB431542 represent a promising tool for directing stem cell fate towards neural lineages and inducing early neural structures.

2.5. Dual-SMAD inhibition signaling pathway for neural induction of hiPSCs

Based on the previous immunofluorescence staining results, we confirmed that small molecule-loaded nanoparticles are effective in promoting neural differentiation. Therefore, we further investigated the effects of nanoparticles loaded with various small molecules on gene expression and specific signaling pathways in neural development. Quantitative PCR analysis on day 1 of the experiment revealed a significant upregulation of SOX1 expression in the LDN@MSN-CaP group,

showing approximately a 2.8-fold increase (±0.2-fold) compared to the control group, indicating a robust induction of neural differentiation. In contrast, the SB@MSN-CaP group showed a moderate increase in PAX6 expression, approximately 1.5-fold (±0.1). The treatment with nanoparticles loaded with two different small molecules (LDNSB@MSN-CaP) produced an additive effect, enhancing PAX6 expression by approximately 1.8-fold (±0.15) compared to the control. The nanoparticle-treated group exhibited relatively lower OCT4 expression compared to the control group, although this difference was not statistically significant. By day 5, SOX1 expression in the LDN@MSN-CaP group was markedly elevated, approximately 16-fold (±0.4), reflecting sustained neural differentiation. PAX6 expression peaked in both the LDN@MSN-CaP and LDNSB@MSN-CaP groups, achieving approximately 12-fold (±0.3) and 10-fold (±0.3) increases, respectively, underscoring the potent induction of neural differentiation markers over time. Conversely, OCT4 expression was significantly decreased across all groups, indicating a loss of pluripotency as differentiation progressed (Fig. 7A and B). Additionally, we found that LDN@MSN-CaP- and LDNSB@MSN-CaP-treated hiPSCs showed significantly decreased activation of Smad1/5/9 compared to the control and SB@MSN-CaP groups. We also observed that in the groups treated with LDN@MSN-CaP and LDNSB@MSN-CaP, the activation of Smad1/5/9 was significantly suppressed. Both groups consistently exhibited reduced pSMAD1/5/9 expression by day 5, confirming the effective inhibition of the BMP signaling pathway and the subsequent promotion of neural differentiation. In contrast, no suppression of pSMAD1/5/9 was observed in the group treated with SB@MSN-CaP, supporting the notion that BMP signaling inhibition was primarily mediated by LDN193189. Interestingly, there was no statistically significant difference in SMAD2/3

activation among the nanoparticle-treated groups at both day 1 and day 5. SMAD2/3 is activated by TGF-β signaling, which promotes differentiation into glial cells, whereas SB431542 is used to inhibit this pathway and induce neural differentiation. In this study, despite treating the cells with SB431542-loaded nanoparticles, the suppression of SMAD2/3 activation appeared to be insufficient (Fig. S2A†). As shown in Fig. S2B,† we hypothesize that this can be attributed to the overexpression of endogenous TGF-β, which continuously stimulates SMAD2/3 signaling, thus impeding the effective suppression of SMAD2/3 activation.

The results of this study not only reinforce the role of dual inhibition in promoting neural differentiation but also demonstrate significant improvements compared to previous research. In prior studies, the individual inhibition of BMP and TGF-β pathways achieved moderate success in inducing neural markers, such as SOX1 and PAX6, but these effects were often limited in magnitude and efficiency.[40] In contrast, the current approach using LDN193189 and SB431542 encapsulated within MSN-CaP nanocarriers has substantially produced enhanced neural differentiation outcomes. In particular, the dramatic upregulation of SOX1 (~16-fold on day 5) and PAX6 (~12-fold on day 5) in the combination treatment group (LDNSB@MSN-CaP) represented a marked improvement over previous reports, where such levels of neural marker expression were typically lower.[41] Moreover, the synchronized and controlled release of these inhibitors through nanocarrier systems can contribute to the sustained and amplified differentiation effect, leading to a more efficient and accelerated commitment to a neural fate. This is in contrast to prior methodologies, which often rely on transient exposure or free-form small molecules, resulting in less consistent outcomes. Selective inhibition of BMP and TGF-β pathways in neural
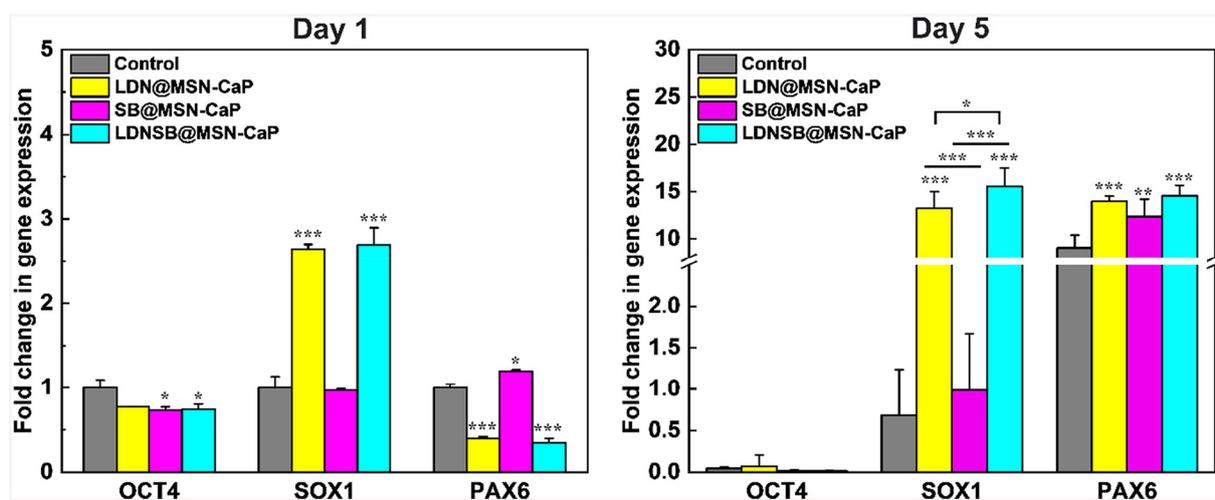

Fig. 7 Small molecule-encapsulated MSN-CaP nanoparticles differentially regulating gene expression in hiPSCs. RT-qPCR analysis of OCT4, SOX1 and PAX6 during dual-SMAD inhibition reveals neural differentiation for 1 day and 5 days. Relative quantification by RT-qPCR of mRNA expression levels of the genes evaluated at different times (day 1 and day 5) compared with day 1 and normalized with the expression of the reference gene (GAPDH). Values are presented as mean ± SEM. Statistical significance is indicated as *$p < 0.05$, **$p < 0.01$, and ***$p < 0.001$, as measured using unpaired Student's *t*-test.

differentiation was further elucidated through the analysis of SMAD protein expression. In both the LDN@MSN-CaP and LDNSB@MSN-CaP groups, pSMAD1/5/9 levels were significantly reduced on both day 1 and day 5, indicating effective inhibition of the BMP pathway. This inhibition aligns with the increased expression of neural differentiation markers and supports the established understanding that BMP suppression plays a critical role in promoting neural lineage transition. Interestingly, the expression levels of pSMAD2/3 did not show significant differences between the SB@MSN-CaP and LDNSB@MSN-CaP groups at any time point, suggesting more complex interactions within the TGF-β pathway. The data imply that while the TGF-β pathway is partially inhibited, the presence of endogenously secreted TGF-β proteins can maintain a baseline level of pathway activity. Such nuanced regulation could be crucial for promoting differentiation while preventing premature or incomplete lineage commitment. Additionally, the phosphorylation patterns of SMAD proteins (SMAD1/5/9 and SMAD2/3) suggest a more precise modulation of signaling pathways, particularly when both inhibitors are delivered together. Previous studies using LDN193189 and SB431542 in free form demonstrated pathway inhibition but often lacked this level of pathway-specific control, likely due to issues related to dosage regulation and timing.[14,42] The use of nanocarriers ensures more efficient uptake and controlled inhibitor release, enhancing the specificity of pathway targeting and contributing to superior neural differentiation results.[43,44] In summary, the current study surpasses earlier research by offering a more effective and controlled approach for dual-pathway inhibition, resulting in higher expression levels of key neural differentiation markers and better signaling pathway modulation. This underscores the potential of nanoparticle-based delivery systems for stem cell differentiation strategies and provides a more robust foundation for future applications in neural regeneration and tissue engineering. Further exploration of long-term differentiation effects and *in vivo* applications could reveal even greater advantages of this approach.

3. Conclusion

This study demonstrates the development of dual-stimuli-responsive MSN-CaP nanoparticles as an effective platform for enhancing the neural differentiation of hiPSCs. Encapsulating the BMP and TGF-β inhibitors, LDN193189 and SB431542, enabled precise and controlled release in response to pH- and GSH-sensitive conditions. This dual inhibition approach significantly improved neural differentiation, as evidenced by the increased expression of neural markers PAX6 and SOX1 and the formation of neural rosette structures, particularly in the LDNSB@MSN-CaP-treated group. Controlled delivery of these inhibitors allowed for more precise modulation of SMAD signaling pathways, leading to superior differentiation outcomes compared to traditional free-form inhibitor methods. The results highlight the potential of MSN-CaP nanoparticles as a

scalable and efficient system for promoting neural lineage commitment. The dual-stimuli-responsive delivery system addresses critical challenges in stem cell-based neural therapies by offering enhanced control and efficiency. The robust induction of neural progenitors and the formation of organized neural structures suggest potential applications in studying neurodegenerative diseases, spinal cord injury, and regenerative tissues. Moreover, the proposed method provides a scalable and precise platform for neural differentiation, which holds significant potential for clinical applications in regenerative medicine. This includes the treatment of neurodegenerative diseases, such as Parkinson's or Alzheimer's disease, and spinal cord injuries. By minimizing off-target effects, the controlled release system could pave the way for safer and more effective stem cell therapies. Further studies are needed to investigate the long-term differentiation and functional integration of derived neural cells, as well as the *in vivo* efficacy of this system in regenerative medicine. Overall, this dual-pathway inhibition strategy, combined with the advantages of nanoparticle-based delivery, provides a promising foundation for advancing stem cell-based therapies for neurological conditions.

4. Materials and methods

4.1. Chemicals and reagents

Tetraethyl orthosilicate (TEOS), hexadecyltrimethylammonium *p*-toluenesulfonate (CTATos), hydrochloric acid (HCl), triethanolamine (TEA), 3-aminopropyltriethoxysilane (APTES), succinic anhydride, LDN193189 hydrochloride (LDN), SB431542 hydrate (SB), glutathione (GSH), dimethyl sulfoxide (DMSO), fluorescein 5(6)-isothiocyanate (FITC), paraformaldehyde, bovine serum albumin, RIPA buffer and BSA buffer were purchased from Sigma Aldrich GmbH (Germany). Bis[3-(triethoxysilyl) propyl] tetrasulfide (BTES) was purchased from Gelast, Inc. (USA). Calcium nitrate tetrahydrate (Ca(NO$_3$)$_2$·4H$_2$O) and ammonium phosphate ((NH$_4$)$_2$HPO$_4$) were purchased from Daejung Chemicals & Materials. Co. Ltd (Korea). Geltrex, [3-(4,5-dimethylthiazol-2-yl)-2,5-diphenyltetrazolium bromide] (MTT) and ECL solution were purchased from Thermo Fisher Scientific (USA). mTeSR1 was purchased from Stem Cell Technologies (Canada). Triton X-100 was purchased from Samchun (Korea). M Rho-associated kinase (ROCK) inhibitor Y-27632 was purchased from Tocris Bioscience (UK). LysoTracker® Red DND-99 probes, Alexa Fluor 488 goat anti-mouse IgG, Alexa Fluor 594 donkey anti-rabbit IgG and anti-β actin were purchased from Invitrogen (USA). Anti-OCT4 and anti-PAX6 were purchased from Abcam (UK). Rabbit anti-SMAD4, rabbit anti-phospho SMAD1/5/9, rabbit anti-SMAD2/3 and rabbit anti-phospho SMAD2/3 were purchased from Cell Signaling Technology (USA). Rabbit anti-SMAD1/5/9 was purchased from MyBioSource (USA).

4.2. MSN synthesis and modification

MSNs were synthesized using the Stöber method.[45,46] Briefly, CTATos (0.263 g, 0.58 mmol), a mesopore structure-directing

agent, was mixed with TEA (50 μL) in deionized water (DW, 13.7 mL) in a 100 mL flask and stirred at 1000 rpm at 80 °C for 30 minutes. TEOS (1.8 mL) and BTES (180 μL) were then added dropwise and the reaction was continued at 85 °C for 2 hours. After the mixture was cooled, MSNs were collected by centrifugation (12 000 rpm, 10 min) and washed with DW and ethanol. The template surfactant was removed by solvent extraction.[47,48] The MSN pellet was resuspended in 45 mL of methanolic solution with 5 mL of 1 M HCl, heated to 95 °C under reflux for 12 hours, washed with DW and ethanol, and dried in a vacuum oven at 80 °C. To introduce amine groups, 100 mg of MSNs were dispersed in 100 mL of ethanol, refluxed for 12 hours at 85 °C, and treated with 1 mL of APTES. After centrifugation and washing, the amine-functionalized MSNs (MSN-NH$_2$) were dried in a vacuum oven. For carboxylic acid functionalization, 50 mg of MSN-NH$_2$ was dispersed in 20 mL of acetone and 0.1 g of succinic anhydride in 5 mL of acetone was added. After stirring for 24 hours, the MSN-COOH was centrifuged, washed, and dried in a vacuum oven.

4.3. Synthesis of MSN-CaP

10 mg of MSN-COOH nanoparticles were dispersed in 6 mL of DW. The solution's pH was adjusted to 10 using an ammonium hydroxide (NH$_3$) solution to promote the formation of CaP. 10 mg of Ca(NO$_3$)$_2$·4H$_2$O dissolved in 2 mL of DW was added dropwise under stirring to facilitate controlled introduction of calcium ions. The mixture was stirred for 2 hours to allow for efficient binding of calcium ions to the MSN-COOH surface. Subsequently, 6 mg of (NH$_4$)$_2$HPO$_4$ dissolved in 2 mL of DW was added dropwise under stirring to introduce phosphate ions. The final solution was stirred for an additional 24 hours to ensure the complete formation of CaP coating on the MSNs. Finally, MSN-CaP nanoparticles were collected by centrifugation, washed three times with DW and ethanol to remove any unbound precursors or impurities, and then freeze-dried.

4.4. Small molecule loading into MSN-CaP

For loading small molecule compounds (*e.g.*, LDN193189 or SB431542) into MSN-CaP, the small molecule (2 mg) was dissolved in a mixture of DMSO (226 μL for LDN and 260 μL for SB) and DW (774 μL for LDN and 740 μL for SB).[49] The MSN-CaP nanoparticles (10 mg) were dispersed in 8 mL of DW and sonicated until thoroughly dispersed. The small molecule solution was then added dropwise to the MSN-CaP solution under stirring at room temperature (600 rpm) for 23 hours. After the loading process, the mixture was washed with DW and centrifuged at 14 000 rpm for 10 minutes. The supernatant was collected to quantify the amount of unloaded small molecules, and the resulting small molecule-loaded nanoparticles (LDN@MSN-CaP or SB@MSN-CaP) were freeze-dried. For co-loading LDN193189 and SB431542 into MSN-CaP nanoparticles (LDNSB@MSN-CaP), both small molecules were dissolved in separate DMSO and DW mixtures as described above. The MSN-CaP solution was sonicated, and then both LDN and SB solutions were simultaneously added dropwise to

the MSN-CaP solution under stirring for 23 hours. The subsequent washing, centrifugation, and freeze-drying steps were performed following the same protocol as for single-small molecule loading.

4.5. Characterization of MSN-CaP

The morphology, size, and elemental composition of the MSN-CaP nanoparticles were analyzed using transmission electron microscopy (TEM, JEOL-2100F) operating at an acceleration voltage of 200 kV. Additionally, energy-dispersive X-ray spectroscopy (EDX) was performed on the same TEM instrument to obtain elemental mapping information of the nanoparticles. Dynamic light scattering (DLS) using a Zetasizer Nano ZS90 (Malvern Instruments) was performed to determine the hydrodynamic size of the MSN-CaP nanoparticles in solution. The specific surface area and pore characteristics of the nanoparticles were investigated by performing nitrogen adsorption–desorption isotherm measurements at −196 °C using an ASAP 2020 micropore system (Micromeritics Instruments Corp.). The crystalline structure and phase composition of the synthesized MSN-CaP nanoparticles were elucidated using X-ray diffraction (XRD) analysis with Cu Kα radiation (λ = 1.54059 Å) in the range of 10° ≤ 2θ ≤ 70° using an Ultima IV (Rigaku) diffractometer. Zeta potential measurements were performed using a Zetasizer Nano ZS90 (Malvern Instruments) to assess the surface charge of the nanoparticles for various samples including MSNs, MSN-NH$_2$, MSN-COOH, MSN-CaP, LDN193189, LDN@MSN-CaP, SB431542, SB@MSN-CaP, and LDNSB@MSN-CaP.

4.6. Small molecule release test

To compare the small molecule release characteristics of LDN@MSN-CaP, SB@MSN-CaP, and LDNSB@MSN-CaP nanoparticles as a function of pH environment, they were suspended in pH 7.4 and pH 5.0 phosphate-buffered saline (PBS) solutions at a concentration of 1 mg mL^{-1} and stored at 37 °C for 24 hours. Portions of the nanoparticle suspensions were sampled at 0.5, 1, 3, 6, 12, and 24 hour intervals. The samples were centrifuged at 14 000 rpm for 10 minutes to separate the nanoparticles and supernatant. The concentrations of LDN and SB released from the supernatant were measured using UV-VIS spectroscopy. The concentrations were calculated by measuring the absorbance at 230 nm for LDN and 323 nm for SB. Representative UV-VIS spectra for LDN and SB, highlighting their distinct absorbance peaks, are provided in Fig. S3† to validate the accuracy and reliability of the quantification method. The measured concentrations were subsequently used to construct cumulative release profiles for each nanoparticle type.

4.7. Observation of the degradation of dual-stimuli (pH/GSH)-responsive MSN-CaP

To observe the degradation characteristics of pH/GSH dual-stimuli-responsive MSN-CaP nanoparticles, they were suspended in pH 5.0 and pH 7.4 PBS solutions at a concentration of 1 mg mL^{-1}. The nanoparticle suspensions were divided into

two groups: treated with 4 mM GSH solution or untreated.[36] All nanoparticle suspensions were stored at 37 °C for 24 hours. Aliquots from each group were dropped onto TEM sample grids, dried, and subjected to TEM analysis.

4.8. hiPSC culture

Thawed WTC11 hiPSCs were maintained on 6-well plates coated with 1% Geltrex in mTeSR1 culture medium with daily medium replacement. All experiments were performed using hiPSCs between passages 50 and 60. The detailed methods for cell culture and maintenance were described by a previous study.[20] Before cell seeding, the pellet was washed with mTeSR1 medium supplemented with 10 μM ROCK inhibitor Y-27632 to increase cell survival. After 24 hours, the medium was exchanged with mTeSR1 medium without the ROCK inhibitor.

4.9. Cytotoxicity test

For the quantitative analysis of cell viability, the MTT assay was performed. Following nanoparticle treatment, fresh medium with the MTT was added to the cells and carefully aspirated after 4 hours. The internalized purple formazan crystals were dissolved in 100 μL of dimethyl sulfoxide (DMSO) to prepare stock solutions. The absorbance of the stock solutions was measured using a microplate reader (Bio-rad) at a wavelength of 595 nm. The viability of cells was calculated as the percentage of viable cells in the test group (LDN@MSN-CaP, SB@MSN-CaP, and LDNSB@MSN-CaP) relative to the control group using the following equation:

$$\text{Cell viability (\%)} = \frac{\text{OD test group}}{\text{OD control group}} \times 100 \ (\%)$$

4.10. Cellular uptake analysis of MSN-CaP

The intracellular tracking was achieved by labeling MSN-CaP with fluorescein-5-isothiocyanate (FITC). The successful conjugation is attributed to the strong reactivity of the amine group on the surface of MSNs and the thiocyanate group of FITC. Specifically, 30 mg of MSN-NH$_2$ were dispersed in 10 mL of ethanol solution and combined with 6 mL of FITC solution (0.3 mg mL^{-1}). After overnight stirring, the FITC-linked MSN-NH$_2$ was subjected to centrifugation and washed thrice until the supernatants became colorless.[50] The resulting FITC-linked MSN-CaP sample was prepared following the aforementioned methods. Briefly, the cells were seeded at a density of 5 × 10^4 cells per mL in mTeSR1 medium on Geltrex-coated plates to obtain 100% confluency within 2 days after seeding. To compare the effect of cellular uptake, we treated 20 μg mL^{-1} of MSN-CaP overnight. Immunostaining images were captured with a stimulated emission depletion (STED) microscope (Abbeiror).

4.11. Neural induction of hiPSCs treated with small molecule-encapsulated MSN-CaP

For neural induction, hiPSCs were cultured with LDN@MSN-CaP, SB@MSN-CaP, and LDNSB@MSN-CaP for 1

day and 5 days. The hiPSCs were induced to differentiate into neural lineages as previously described with modifications. The medium was changed to neural induction medium, which contains Dulbecco's modified Eagle's medium (DMEM)/F12 containing 1% N2 and 2% B27 supplemented with LDN@MSN-CaP, SB@MSN-CaP, and LDNSB@MSN-CaP. The medium was changed every day for 5 days.

4.12. Immunofluorescence analysis

The cells were fixed with 4% paraformaldehyde for 30 min at room temperature. Following PBS washing, the fixed cells were permeabilized using 0.1% Triton X-100 for 30 min at room temperature, blocked with 3% bovine serum albumin for 1 hour, and then incubated with primary antibody overnight at 4 °C. Primary antibodies against the following proteins were used to characterize diverse cell types: anti-OCT4 (1 : 200) and anti-PAX6 (1 : 200) diluted in PBS. After incubating overnight, the samples were gently rinsed with PBS and incubated with the secondary antibodies Alexa Fluor 488 goat anti-mouse IgG (1 : 200) and Alexa Fluor 594 donkey anti-rabbit IgG (1 : 200) overnight at 4 °C. Each sample was washed with PBS and counterstained with 4′,6-diamidino-2-phenylindole (DAPI, 1 mg mL^{-1} diluted in staining solution) for 10 min at room temperature. Immunostaining images were captured with an inverted confocal laser scanning microscope (LSM710, Carl Zeiss). Image J software was employed for the analysis of the fluorescence intensity in the confocal images.

4.13. Real-time quantitative PCR analysis (qRT-PCR)

The neural induction of hiPSCs treated with molecule-encapsulated MSN-CaP was assessed by measuring DNA content at days 1 and 5 using DNA assay kits according to the protocol. We analyzed the expression of neural induction markers in hiPSCs treated with LDN@MSN-CaP, SB@MSN-CaP, and LDNSB@MSN-CaP for 1 day and 5 days using a StepOnePlus Real-Time PCR System (Applied Biosystems). For total mRNA extraction, RNeasy mini kit (Qiagen) was used and the purity of the extracted mRNA was confirmed using a NanoDrop spectrophotometer (Nabi). cDNA was synthesized from 1 μL of RNA using a cDNA PrimeScript™ 1st strand cDNA synthesis kit (TaKaRa) according to the manufacturer's instructions. Subsequently, 1 μL of cDNA was mixed with SYBR Green Premix (TaKaRa) and primers with specific sequences. All primers used for qPCR assays are listed in Table 1. The parameters of qPCR were fixed for 40 cycles with melting at 95 °C for 15 s, annealing, extension at 60 °C for 60 s, and then extending at 62 °C. The relative expression values of all groups were normalized with the control group.

4.14. Western blotting analysis

The cells were lysed with RIPA buffer. For the western blot analysis, cell lysates were separated by electrophoresis on SDS/PAGE and transferred to a PVDF membrane with a Mini trans-Blot (Biorad). The membrane was blocked with BSA buffer for 1 hour, incubated with a primary antibody diluted in blocking buffer overnight at 4 °C, and then incubated with a primary

Table 1 Primers used in gene expression analysis by qRT-PCR

Primer names	Species	Primer sequence 5′ to 3
OCT4	Human	Forward: GGAGGAAGCTGACAACAATGAAA Reverse: GGCCTGCACGAGGGTTT
SOX1	Human	Forward: TACAGCCCCATCTCCAACTC Reverse: GCTCCGACTTCACCAGAGAG
PAX6	Human	Forward: TGGCCACGTACAGGACCCTC Reverse: CTTGGGGTCCTGAAAGCTGAG
β-Actin	Human	Forward: AGCACAGAGCCTCGCCTT Reverse: CATCATCCATGGTGAGCTGG

antibody overnight at 4 °C. Primary antibodies against the following proteins were used to characterize various cell types: rabbit anti-SMAD4 (1 : 1000), rabbit anti-SMAD1/5/9 (1 : 1000), rabbit anti-phosphoSMAD1/5/9 (1 : 1000), rabbit anti-SMAD2/3 (1 : 1000), rabbit anti-phospho SMAD2/3 (1 : 1000), and anti-β actin (1 : 2000) diluted in PBS. After incubating overnight, the samples were gently rinsed with TBS-T and the membrane was incubated with the secondary antibody goat anti-rabbit IgG (1 : 1000) overnight at 4 °C. After washing with TBS-T, the ECL solution was used for the detection of proteins. The visualization of proteins was performed using a ChemiDoc™ XRS+ (Biorad). Image J software was employed for the analysis of the signal intensity in the western blot images.

Author contributions

Jeong Hyun You: writing – original draft, methodology, investigation, data curation, and conceptualization. Na Yeon Kim: writing – original draft, methodology, and investigation. Yoon Young Choi: writing – original draft, methodology, and investigation. Hyung Woo Choi: analysis and conceptualization. Bong Geun Chung: writing – review & editing, supervision, project administration, and conceptualization. Jeong Hyun You and Na Yeon Kim equally contributed to this work.

Data availability

Original data are available from the corresponding author upon reasonable request.

Conflicts of interest

The authors declare that they have no known competing financial interests or personal relationships that could have appeared to influence the work reported in this paper.

Acknowledgements

References

1 J. G. Roth, M. S. Huang, T. L. Li, V. R. Feig, Y. Jiang, B. Cui, H. T. Greely, Z. Bao, S. P. Pasca and S. C. Heilshorn, *Nat. Rev. Neurosci.*, 2021, **22**, 593–615.

2 A. A. Galiakberova and E. B. Dashinimaev, *Front. Cell Dev. Biol.*, 2020, **8**, 815.

3 S. George, M. R. Hamblin and H. Abrahamse, *Stem Cell Rev. Rep.*, 2019, **15**, 814–826.

4 A. M. Pasca, S. A. Sloan, L. E. Clarke, Y. Tian, C. D. Makinson, N. Huber, C. H. Kim, J. Y. Park, N. A. O'Rourke, K. D. Nguyen, S. J. Smith, J. R. Huguenard, D. H. Geschwind, B. A. Barres and S. P. Pasca, *Nat. Methods*, 2015, **12**, 671–678.

5 D. Ye, Q. Wang, Y. X. Yang, B. Y. Chen, F. Zhang, Z. Y. Wang and Z. Luan, *Cell. Mol. Neurobiol.*, 2023, **43**, 2337–2358.

6 E. Abranches, M. Silva, L. Pradier, H. Schulz, O. Hummel, D. Henrique and E. Bekman, *PLoS One*, 2009, **4**, e6286.

7 M. Wattanapanitch, N. Klincumhom, P. Potirat, R. Amornpisutt, C. Lorthongpanich, U. P. Y. C. Laowtammathron, P. Kheolamai, N. Poungvarin and S. Issaragrisil, *PLoS One*, 2014, **9**, e106952.

8 E. Kawase and N. Nakatsuji, *Biomater. Sci.*, 2023, **11**, 2974–2987.

9 R. Rust, R. Z. Weber, M. Generali, D. Kehl, C. Bodenmann, D. Uhr, D. Wanner, K. J. Zurcher, H. Saito, S. P. Hoerstrup, R. M. Nitsch and C. Tackenberg, *J. Transl. Med.*, 2022, **20**, 421.

10 J. Yoon, H. Han and J. Jang, *Nano Convergence*, 2023, **10**, 52.

11 K. Liu, C. Yu, M. Xie, K. Li and S. Ding, *Cell Chem. Biol.*, 2016, **23**, 893–916.

12 I. Tortorella, C. Argentati, C. Emiliani, F. Morena and S. Martino, *Cells*, 2022, **11**, 3093.

13 N. K. Jha, W. C. Chen, S. Kumar, R. Dubey, L. W. Tsai, R. Kar, S. K. Jha, P. K. Gupta, A. Sharma, R. Gundamaraju, K. Pant, S. Mani, S. K. Singh, R. B. Maccioni, T. Datta, S. K. Singh, G. Gupta, P. Prasher, K. Dua, A. Dey, C. Sharma, Y. H. Mughal, J. Ruokolainen, K. K. Kesari and S. Ojha, *Open Biol.*, 2022, **12**, 210289.

14 Y. Qi, X. J. Zhang, N. Renier, Z. Wu, T. Atkin, Z. Sun, M. Z. Ozair, J. Tchieu, B. Zimmer, F. Fattahi, Y. Ganat,

R. Azevedo, N. Zeltner, A. H. Brivanlou, M. Karayiorgou, J. Gogos, M. Tomishima, M. Tessier-Lavigne, S. H. Shi and L. Studer, *Nat. Biotechnol.*, 2017, **35**, 154–163.

15 R. H. Xu, T. L. Sampsell-Barron, F. Gu, S. Root, R. M. Peck, G. J. Pan, J. Y. Yu, J. Antosiewicz-Bourget, S. L. Tian, R. Stewart and J. A. Thomson, *Cell Stem Cell*, 2008, **3**, 196–206.

16 S. M. Chambers, Y. Mica, G. Lee, L. Studer and M. J. Tomishima, *Methods Mol. Biol.*, 2016, **1307**, 329–343.

17 L. Nie, D. Yao, S. Chen, J. Wang, C. Pan, D. Wu, N. Liu and Z. Tang, *Cell Death Discovery*, 2023, **9**, 215.

18 C. D. Rogers, S. A. Moody and E. S. Casey, *Birth Defects Res., Part C*, 2009, **87**, 249–262.

19 M.-L. Zou, Z.-H. Chen, Y.-Y. Teng, S.-Y. Liu, Y. Jia, K.-W. Zhang, Z.-L. Sun, J.-J. Wu, Z.-D. Yuan and Y. Feng, *Front. Mol. Biosci.*, 2021, **8**, 593310.

20 N. Y. Kim, Y. Y. Choi, T. H. Kim, J. H. Ha, T. H. Kim, T. Kang and B. G. Chung, *ACS Appl. Mater. Interfaces*, 2024, **16**, 15730–15740.

21 A. Gupta and S. Singh, *Mol. Neurobiol.*, 2022, **59**, 983–1001.

22 H. I. Seo, A. N. Cho, J. Jang, D. W. Kim, S. W. Cho and B. G. Chung, *Nanomedicine*, 2015, **11**, 1861–1869.

23 A. Abdal Dayem, E. Yan, M. Do, Y. Kim, Y. Lee, S. G. Cho and D. H. Kim, *Nano Convergence*, 2024, **11**, 24.

24 Y. Zou, B. Huang, L. Cao, Y. Deng and J. Su, *Adv. Mater.*, 2021, **33**, e2005215.

25 R. S. Guimaraes, C. F. Rodrigues, A. F. Moreira and I. J. Correia, *Pharmacol. Res.*, 2020, **155**, 104742.

26 W. Fan, N. Lu, Z. Shen, W. Tang, B. Shen, Z. Cui, L. Shan, Z. Yang, Z. Wang, O. Jacobson, Z. Zhou, Y. Liu, P. Hu, W. Yang, J. Song, Y. Zhang, L. Zhang, N. M. Khashab, M. A. Aronova, G. Lu and X. Chen, *Nat. Commun.*, 2019, **10**, 1241.

27 P. Sutthavas, Z. T. Birgani, P. Habibovic and S. van Rijt, *Adv. Healthc. Mater.*, 2022, **11**, 2101588.

28 H. P. Rim, K. H. Min, H. J. Lee, S. Y. Jeong and S. C. Lee, *Angew. Chem., Int. Ed.*, 2011, **50**, 8853–8857.

29 S. P. Hadipour Moghaddam, J. Saikia, M. Yazdimamaghani and H. Ghandehari, *ACS Appl. Mater. Interfaces*, 2017, **9**, 21133–21146.

30 M. Wu, Q. Meng, Y. Chen, Y. Du, L. Zhang, Y. Li, L. Zhang and J. Shi, *Adv. Mater.*, 2015, **27**, 215–222.

31 H. K. Choi, M. Z. Chen, L. Goldston and K. B. Lee, *Nano Convergence*, 2024, **11**, 19.

32 Y. Ma, Z. Su, L. Zhou, L. He, Z. Hou, J. Zou, Y. Cai, D. Chang, J. Xie, C. Zhu, W. Fan, X. Chen and S. Ju, *Adv. Mater.*, 2022, **34**, e2107560.

33 Z. A. Alothman, *Materials*, 2012, **5**, 2874–2902.

34 K. Y. Chen and Y. Arai, *ACS Earth Space Chem.*, 2019, **3**, 2266–2275.

35 S. Kojima, H. Nakamura, S. Lee, F. Nagata and K. Kato, *Int. J. Mol. Sci.*, 2019, **20**, 4650.

36 H. W. Choi, J. H. Lim, T. Kang and B. G. Chung, *Antioxidants*, 2022, **11**, 1335.

37 Y. Elkabetz and L. Studer, *Cold Spring Harbor Symp. Quant. Biol.*, 2008, **73**, 377–387.

38 R. Rahimi Darehbagh, M. Mahmoodi, N. Amini, M. Babahajiani, A. Allavaisie and Y. Moradi, *Eur. J. Med. Res.*, 2023, **28**, 576.

39 V. Asgari, A. Landarani-Isfahani, H. Salehi, N. Amirpour, B. Hashemibeni, S. Rezaei and H. Bahramian, *Neurochem. Res.*, 2019, **44**, 2695–2707.

40 S. M. Chambers, C. A. Fasano, E. P. Papapetrou, M. Tomishima, M. Sadelain and L. Studer, *Nat. Biotechnol.*, 2009, **27**, 275–280.

41 P. Walsh, V. Truong, S. Nayak, M. S. Montivero, W. C. Low, A. M. Parr and J. R. Dutton, *Stem Cells*, 2020, **38**, 1400–1408.

42 M. Li, Y. Zou, Q. Lu, N. Tang, A. Heng, I. Islam, H. J. Tong, G. S. Dawe and T. Cao, *J. Biomed. Sci.*, 2016, **23**, 34.

43 L. Zhu, W. Zhong, X. Meng, X. Yang, W. Zhang, Y. Tian and Y. Li, *J. Nanobiotechnol.*, 2024, **22**, 424.

44 C. N. Ko, S. Zang, Y. Zhou, Z. Zhong and C. Yang, *J. Nanobiotechnol.*, 2022, **20**, 380.

45 H. Y. Chiu, W. Deng, H. Engelke, J. Helma, H. Leonhardt and T. Bein, *Sci. Rep.*, 2016, **6**, 25019.

46 S. G. Balwe, D. Moon, M. Hong and J. M. Song, *Nano Convergence*, 2024, **11**, 48.

47 H. Ghaedi and M. Zhao, *Energy Fuels*, 2022, **36**, 2424–2446.

48 J. Han, J. Lim, C. J. Wang, J. H. Han, H. E. Shin, S. N. Kim, D. Jeong, S. H. Lee, B. H. Chun, C. G. Park and W. Park, *Nano Convergence*, 2023, **10**, 36.

49 A. Samara, M. Falck, M. Spildrejorde, M. Leithaug, G. Acharya, R. Lyle and R. Eskeland, *STAR Protoc.*, 2022, **3**, 101533.

50 Z. Wang, Y. Tian, H. Zhang, Y. Qin, D. Li, L. Gan and F. Wu, *Int. J. Nanomed.*, 2016, **11**, 6485–6497.